Magnetic X-points, edge localized modes, and stochasticity[a)]

L. E. Sugiyama[1,b)] and H. R. Strauss[2]
[1]*Laboratory for Nuclear Science, Massachusetts Institute of Technology, Cambridge, Massachusetts 02139-4307, USA*
[2]*HRS Fusion, West Orange, New Jersey 07052, USA*

(Received 15 March 2010; accepted 17 May 2010; published online 25 June 2010)

Edge localized modes (ELMs) near the boundary of a high temperature, magnetically confined toroidal plasma represent a new type of nonlinear magnetohydrodynamic (MHD) plasma instability that grows through a coherent plasma interaction with part of a chaotic magnetic field. Under perturbation, the freely moving magnetic boundary surface with an X-point splits into two different limiting asymptotic surfaces (manifolds), similar to the behavior of a hyperbolic saddle point in Hamiltonian dynamics. Numerical simulation using the extended MHD code M3D shows that field-aligned plasma instabilities, such as ballooning modes, can couple to the "unstable" manifold that forms helical, field-following lobes around the original surface. Large type I ELMs proceed in stages. Initially, a rapidly growing ballooning outburst involves the entire outboard side. Large plasma fingers grow well off the midplane, while low density regions penetrate deeply into the plasma. The magnetic field becomes superficially stochastic. A secondary inboard edge instability causes inboard plasma loss. The plasma gradually relaxes back toward axisymmetry, with diminishing cycles of edge instability. Poloidal rotation of the interior and edge plasma may be driven. The magnetic tangle constrains the early nonlinear ballooning, but may encourage the later inward penetration. Equilibrium toroidal rotation and two-fluid diamagnetic drifts have relatively small effects on a strong MHD instability. Intrinsic magnetic stochasticity may help explain the wide range of experimentally observed ELMs and ELM-free behavior in fusion plasmas, as well as properties of the H-mode and plasma edge. © *2010 American Institute of Physics*.
[doi:10.1063/1.3449301]

I. INTRODUCTION

Most magnetically confined toroidal plasmas for fusion research operate with a bounding magnetic surface whose cross section has one or two "X"-points, at the top or bottom of the plasma, where the magnetic field lines become exactly toroidal. This shape allows good plasma confinement with a steep pressure gradient just inside the plasma edge, the so-called H-mode,[1] although the reason for the improved edge confinement is incompletely understood. High plasma pressure at the top of the gradient is desirable for high fusion reactivity, but it is self-limited by plasma instabilities driven by the pressure gradient (ballooning modes)[2] or by the large local plasma current caused by the pressure gradient (peeling modes).[3,4] X-points allow the plasma boundary to attain a more triangular shape, which provides some stabilization against these modes. They were originally conceived as a means to control the plasma outflux and impurity influx, channeling the outflux along the field lines to special "divertor" regions at the wall. In practice, the plasma loss is less controllable. In many cases periodic edge localized modes[5,6] (ELMs) expel large amounts of plasma particles and energy to the surrounding walls, on fast magnetohydrodynamic (MHD) time scales. Many features of large ELMs are similar across experiments, but others differ.[7–9] In fusion burning plasmas, the power losses can be large enough to be dangerous to the material surfaces. Controlling or eliminating ELMs constitutes one of the most important challenges to next generation fusion burning experiments, such as ITER.[10]

A toroidal magnetic field satisfies $\nabla \cdot \mathbf{B}=0$ and can be described as a Hamiltonian system with two degrees of freedom.[11] For axisymmetric nested magnetic surfaces without X-points, Hamiltonian theory[12,13] predicts that much of the original nested structure is retained under small perturbations. A few isolated magnetic island chains and mixed field regions appear, bounded by Kolmogorov–Arnold–Moser[14] (KAM) surfaces that correspond to original surfaces with irrational field line winding numbers. As the perturbation grows, surviving surfaces are progressively lost, in a predictable way. Much of the theory of toroidal plasmas has been based on this picture.

The plasma boundary is less constrained than interior surfaces. A magnetic X-point on the plasma boundary corresponds to a hyperbolic saddle point in a Hamiltonian system.[15,16] Under small perturbations, the magnetic surface near the X-point splits into two different, multiply intersecting asymptotic limits, as in the Hamiltonian system,[13,17] whose behavior was first noted by Poincare.[18] The X-point itself is a fixed point. The two limiting surfaces (actually, manifolds) can be defined[12,13] as the limiting locations of the field lines as they emanate from or approach the X-point, traced infinitely in each direction. Field lines defining the stable manifold are directed toward the X-point, while on its other side the field lines of the unstable manifold move away from the X-point (cf. Fig. 8).

[a)]Based on an invited presentation at the 51st APS DPP Meeting in Atlanta, Georgia in 2009. Paper PI2 1, Bull. Am. Phys. Soc. **54**, 217 (2009).
[b)]Invited speaker.

In the unperturbed state, the two manifolds coincide on a flux surface. Once a perturbation splits the field and the two manifolds develop a single transverse intersection point, they no longer coincide almost anywhere. Each side of the X-point effectively has two field-line limiting surfaces, one forming loops around the original surface ("unstable") and the other lying near the original ("stable"). Although multiple X-points may exist, much of the ELM dynamics can be captured by considering the two pairs of perturbed manifolds that exist locally on each side of a single X-point.

The perturbed stable and unstable manifolds cannot cross themselves, but can cross each other. The intermediate field lines also intersect. Each secondary X-point formed by intersection also undergoes asymptotic surface splitting as the perturbation grows. The resulting field forms a magnetic tangle with a complex, chaotic structure. (The terms chaotic and stochastic will be used interchangeably for the ELM field, since it deviates from an ideal Hamiltonian tangle.) If the far ends of the stable and unstable manifolds connect to a single X-point, the tangle is called homoclinic or, if to different X-points, heteroclinic.

The unconfined field lines outside the plasma do not form closed surfaces, but typically wind a few times toroidally between their end points on the surrounding walls. In the Hamiltonian picture, such trajectories are classified as unstable and cannot be described by the field splitting arguments that apply to closed surfaces. The unstable perturbed manifold of the boundary projects beyond the original plasma boundary [the last closed flux surface (LCFS)], but does not readily connect to the exterior, unconfined field lines.

Experimental measurements on tokamaks with small, deliberately applied nonaxisymmetric fields [resonant magnetic perturbations (RMPs)[19]] show[20,21] magnetic signatures in the divertor that qualitatively match the field structure predicted for a homoclinic tangle. ELM divertor traces[22–25] are also compatible with a homoclinic tangle. Both show multiple spiraling nonaxisymmetric stripes of plasma heating on the divertor surfaces. The comparisons so far have used only the vacuum magnetic fields, which could be measured directly. The plasma response should change the field and the tangle in important ways. For the RMP, evidence includes experimental comparisons,[20] predictions from MHD simulations,[26,27] and suggestions by particle simulations with the neoclassical code XGC0.[28] Theoretical[29] and experimental studies of stellarators and other helical plasmas also find that the plasma response to nonaxisymmetric perturbations is important.

The ELM generates its own magnetic perturbation. A magnetic tangle was first identified in M3D simulations.[30] It had not been considered in previous analytical or numerical studies (cf. review[8]). The linearized, small perturbation plasma theory[31] does not allow asymptotic field splitting. For linearized ballooning modes, analytical solutions exist only for interior flux surfaces[2,32] and boundary surfaces without X-points.[33] Linear MHD stability codes can solve the linearized equations for X-point boundaries, but without surface splitting. KINX (Ref. 34) assumes a radial displacement $\xi\cdot\nabla\psi=0$ on the boundary flux surface, while ELITE,[35,36] MISHKA-1,[37] and other stability codes evaluate interior magnetic flux surfaces up to more than 99% of the X-point boundary, to converge in the limit to the full fixed boundary result. The linearized limits of nonlinear simulation codes also typically assume a fixed, unsplit boundary.

Nonlinearly, freely moving X-point plasma boundaries are difficult to simulate. Some numerical models use field-line-following or flux-tube approximations[38] or assume limited evolution of the field or plasma current. Many use simplified plasma models, such as reduced MHD, or full MHD with a limited number of toroidal harmonics.[39–41] Almost all use unrealistically large values for the plasma resistivity and other dissipative coefficients compared to experiment, for reasons of numerical stability. Sharp differences between the plasma interior and "vacuum" typically concentrate in a narrow gradient region around the plasma edge and must be reduced.[42] In addition, the formation of a homoclinic tangle depends critically on the Hamiltonian form of the magnetic field, which is guaranteed by $\nabla\cdot\mathbf{B}=0$. Codes that advance vector components of $\mathbf{B}$ in time often find this condition difficult to satisfy accurately. Thus, while all the nonlinear simulations that included a freely moving plasma boundary with an X-point (M3D,[27,30,39] NIMROD,[40] JOREK,[41] and others[42]) saw evidence of field stochastization, its true degree and cause could not be determined.

Experimental observations of ELMs are also limited. Observable regions are limited and vary from experiment to experiment. Many quantities are difficult to measure, particularly inside a hot fusion plasma. Stochastic quantities are even harder. Many measurements have low spatial or temporal resolution compared to the few Alfvén times of MHD evolution. They may integrate along multiple chords through the plasma or over long time intervals, making interpretation difficult.

The M3D code[43,44] is an initial value, extended MHD code that specifically preserves $\nabla\cdot\mathbf{B}=0$. Earlier M3D simulations of large ELMs[27,39] at lower resolution did not consider tangle effects. An upgraded code, at higher spatial resolution, was required.[30]

This paper reports results at more realistic parameters, including the actual, or nearly actual, resistivity. Section II describes the numerical model and the simulation cases. The magnetic tangle leads to a characteristic multistage ELM instability, summarized in Sec. III for a large type I ELM in DIII-D. Section IV illustrates the early nonlinear formation of a characteristic helical, filamentary shape. Section V discusses the ELM stages in terms of a magnetic tangle. Section VI presents some quantitative effects of the tangle on the early ELM, including the scaling of growth with resistivity and the constraining effects of the magnetic tangle on the early ballooning. The final section is a summary.

II. NUMERICAL MODEL

Numerical simulations were carried out with the M3D initial value code,[43] using MHD and two-fluid[44] models. It simulates a plasma with a freely moving boundary, surrounded by a resistive MHD vacuum that is bounded by a rigid, partially conducting wall of infinitesimal thickness.

The vacuum is characterized by low density, zero temperature, and very high resistivity, used to approximate zero current. The magnetic boundary surface of the plasma (last closed flux surface or LCFS) has one X-point on its lower tip. A second X-point is located a short distance outside the plasma, above and inboard of the top. The configuration, including the vacuum field and the wall representing the vacuum vessel, is taken from DIII-D experimental reconstructions using EFIT.[45,46] The wall is slightly smoothed. The paper concentrates on two well-analyzed DIII-D discharges, 119690 at $t=2656$ ms (Refs. 19 and 47) and 126006 at $t=3500$ ms.[48]

Discharge 119690 had an ITER-similar shape, but relatively high plasma density and collisionality, $\nu_e=0.7$. It also had a very steep, narrow edge pressure gradient that was MHD unstable to ballooning-type modes. There were no precursor oscillations. The plasma had toroidal magnetic field $B_T=1.60$ T at major radius $R_o=1.76$ m, current $I_p=1.042$ MA, central density $n_{eo}=1.2\times10^{20}$ m^{-3}, temperature $T_{eo}\simeq T_{io}=1.83$ keV, and normalized $\beta_N=1.81$. The neutral beam heating power was $P_{NB}=4.8$ MW. The edge safety factor was $q_{95}\simeq3.75$. The central value of q_o just above unity made the simulation sensitive to a 1/1 magnetic island, while the experiment had sawteeth during the ELM phase. The $\nabla\mathbf{B}$ drift was toward the lower X-point. The equilibrium included a large, narrow bootstrap current layer along the outboard plasma edge, calculated using the standard DIII-D neoclassical transport method.[46] One caveat is that the "experimental" density profiles over the plasma edge region were not measured directly, but fit using the standard DIII-D tanh function.

Case 119690 was atypical for DIII-D, in that the ELM could be completely stabilized by applying a nonaxisymmetric $n=3$ field (RMP) with odd parity across the midplane,[19,47] instead of the usual even parity. Other cases, with different type I ELMs, were also simulated. These included discharge 126006 at 3500 ms,[48] where ELMs were stabilized by an even parity RMP, and 113317, a Joint European Torus (JET)-shaped H-mode discharge with smaller ELMs. The reference simulation used a wide inboard vacuum layer between the plasma and the wall, with the true wall location approximated as the major radius R where the resistive and viscous dissipation became very large. The other cases used the actual inner wall location, with similar inboard results.

The baseline simulations assume a stationary equilibrium. The actual plasmas had significant equilibrium toroidal rotation.

M3D solves the compressible, resistive MHD equations with density and temperature evolution.[43] The density evolves by the continuity equation, The form of the magnetic field satisfies $\nabla\cdot\mathbf{B}=0$ at every time step.

No fourth order hyper-resistivity or viscosity was used. The diffusive part of the density upwind advection[49] was used for the density and pressure. The diffusion coefficient is proportional to $|v_\perp|dx$ where dx is the length of a segment connecting the midpoint of a triangle edge to the triangle barycenter and $v_\perp$ is the fluid velocity perpendicular to ϕ. The toroidal velocity used the diffusion coefficient $v_\perp^2\ \Delta t$, also related to the upwind advection, for numerical stability.

A large resistive and viscous damping was applied in the vacuum very near the bounding wall. The perpendicular thermal conductivity was also large there.

Typical values of resistivity corresponded to Lundquist numbers $S=3.3\times10^6$ to 3.3×10^7 in the plasma at the top of the edge pedestal. The vacuum $S_{\rm vac}=10^3$. For 119690, $S=3.3\times10^7$ is the actual plasma value, based on $Z_{\rm eff}\simeq3$. The normalized kinematic ion viscosity was typically $\mu_i/\rho=6\times10^{-6}$, and effective thermal diffusivities were $\kappa_\perp=D_n=10^{-5}$ and $\kappa_\parallel=3.53(R_o/a_o)$, modeled by the M3D artificial sound wave method.[43] Code lengths are normalized to $a_o=1$ m. Times are normalized to the Alfvén time $\tau_A=R_o/v_A$, based on the vacuum field and density at the magnetic axis $R=R_o$. For 119690, the reference $\tau_A=0.78\ \mu$s. For 126006, $\tau_A=0.43\ \mu$s.

Most cases used linear triangular finite elements (finite volumes) in the poloidal plane; a few used third order. The spatial grid in each poloidal (constant ϕ) plane was packed around the plasma edge, more tightly on the outboard side. Typical numbers of vertices in one plane ranged from 15 700 to 20 000. The radial packing barely resolved the steep edge density gradient and current density in case 119690, but varying it did not significantly change the results.

The typical range of toroidal mode numbers was $|n|=0$ to 23. A few higher resolution runs with $|n|\leq47$ modes showed that the basic nonlinear instability fell within the lower range.

MHD requires a finite vacuum density to keep the shear Alfvén velocity finite. It was typically taken to be $n_{\rm vac}/n_o=0.1-0.2$, with 0.1 for the reference 119690 case. (The earlier strongly unstable case in Ref. 30 used $n_{\rm vac}/n_o=0.4$.) The vacuum pressure, temperature, and current density were initially zero.

Plasma sources and sinks were neglected, beyond small sources that compensate the diffusion terms to help maintain the equilibrium and a small implicit source to keep $n\geq n_{\rm vac}$. These have little effect over the simulations. Ionization, impurity ions, and wall interactions are beyond the scope of the simulation. Heating was also neglected. The velocity boundary condition at the wall was normal velocity $v_n=0$ with slip tangential velocity, while the density and temperature were held constant. The parallel electrical sheath at the wall was neglected, since MHD is strictly quasineutral. The results suggest that a sheath condition or additional physics may be important, since large localized currents may develop transiently near the wall, a phenomenon also seen in experiment.[50]

The reference simulation for case 119690 used approximately 330 hours on 360 processors on a Cray XT-4 for $600\tau_A$. A shorter simulation of 126006 at higher resolution used approximately 200 hours on 432 processors for $330\tau_A$.

Other uncertainties remain. The experimental data used for the equilibrium may not be completely consistent. Most importantly, the edge pedestal location and plasma profiles may not match exactly. Due to the inevitable constraints on computer time and availability, the simulations were barely resolved numerically, particularly near the X-points. The plasma center had relatively coarse resolution. Toroidal rotation and error fields, important factors in experiment, have

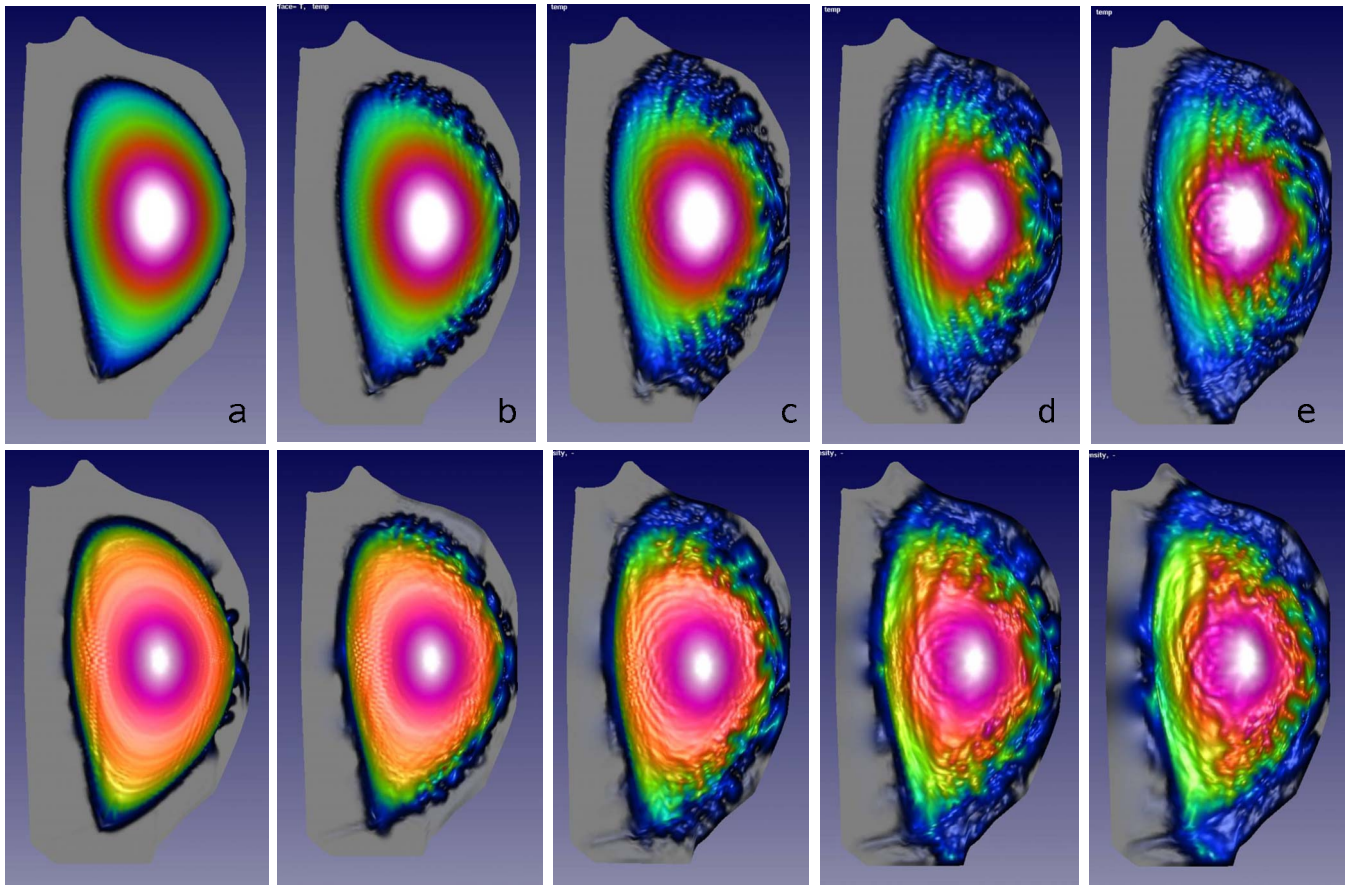

FIG. 1. (Color online) Initial mode and ballooning outburst for an ELM in discharge 119690 with $S=3.3\times10^7$. Contours of temperature (top row) and density (bottom) at (a) $t=21.5\tau_A$, (b) 42.8, (c) 62.3, (d) 83.4, and (e) 104.6. The surrounding light gray region is the vacuum. Ballooning fingers extend rapidly between $t\simeq42.8$ and 62, then slow. The disturbance continues to develop inward.

been largely ignored. In addition, physics beyond extended MHD may be important. Further work is needed to address these issues.

III. MULTISTAGE ELM

The resulting ELM occurs in several stages. This summary is based on the reference DIII-D 119690 case, which was strongly unstable at the actual resistivity $S=3.3\times10^7$. Other DIII-D ELMs were qualitatively similar, with differences of degree. An earlier 119690 case,[30] run at more extreme parameters, shows similar behavior despite an unrealistically strong instability.

The simulation was started with a small random perturbation of all $n\neq0$ toroidal harmonics of the toroidal vorticity $w=(-R_o/R)\hat{\phi}\cdot\nabla\times\mathbf{v}$. Figures 1–6 show the evolution of main instability and part of the healing phase, over $604\tau_A$ or 0.47 ms.

Many features resemble experimental observations.[7,51] Other predictions are new. Important elements include the fundamental filamentary, helical nature of the plasma and magnetic structures near the outboard separatrix, an initial large, rapid plasma ballooning-type outburst over most of the outboard side, followed by a secondary inboard edge instability, plasma loss in concentrated blobs directly to the divertors from both the outboard and inboard sides of the X-points, multiple quasiperiodic cycles of instability and plasma loss with decaying amplitude on both inboard and outboard sides, and eventual healing toward the original axisymmetric configuration.

A. Outboard ballooning instability

The simulation cases were initially MHD unstable to ballooning-type modes. The instability grows in the steep pressure gradient region on the outboard side of the plasma, near the horizontal midplane, shown by the temperature in Fig. 1(a) (the density also shows some small, cold axisym-

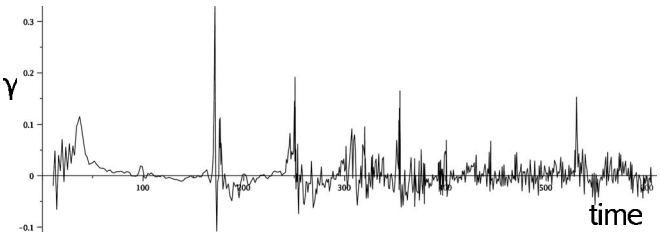

FIG. 2. Volume averaged growth rate γ as a function of time from $t=0$ to $604\tau_A$, for the 119690 reference case. Initial ballooning growth rate peaks by $t\simeq37$ (first peak), then falls, while plasma fingers continue to extend. Outward ballooning subsides by $t\simeq100$ and density clears from the outboard SOL by $t\simeq160$. Large jump at $t\simeq170$ (largest spike) reflects the first large density loss from the inboard midplane. Later quasiperiodic bursts (and small early one near $t\simeq100$) are associated with pulses of inboard density loss.

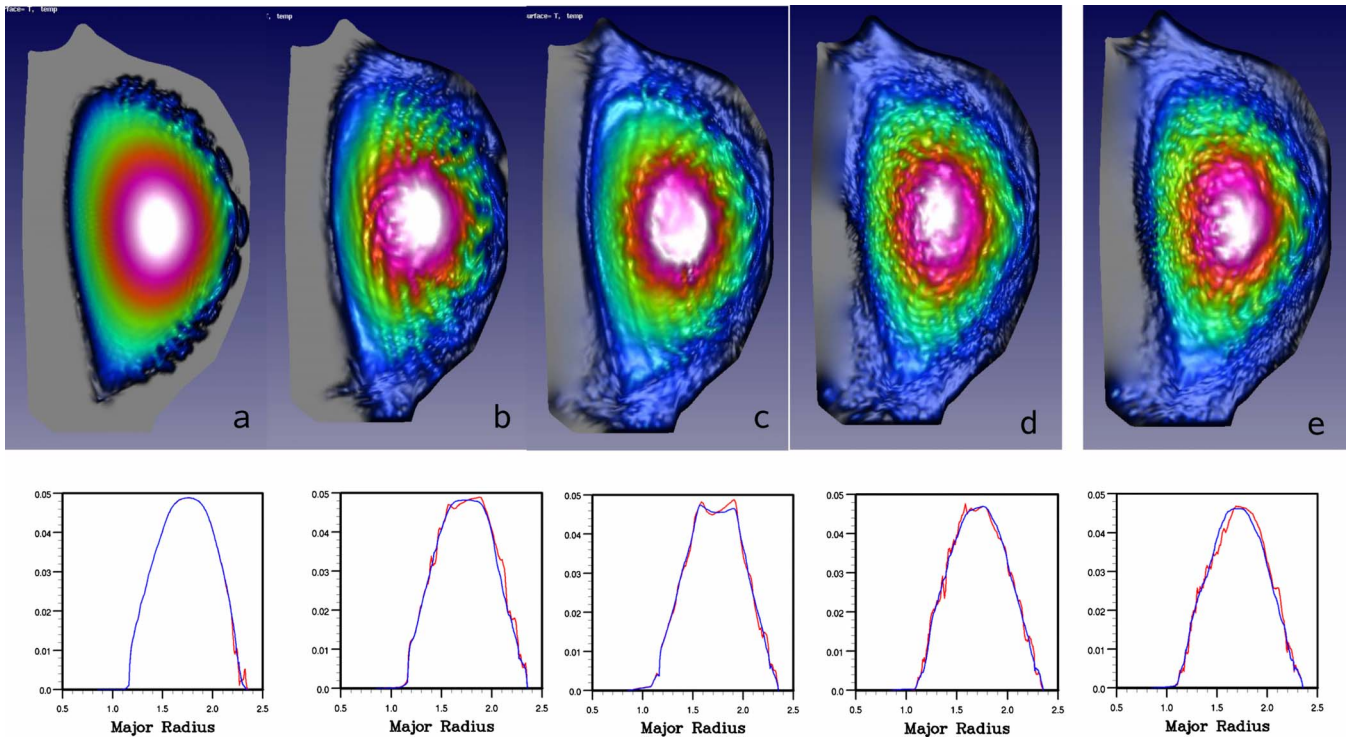

FIG. 3. (Color online) Temperature evolution for the reference case, shown as contours in the plane $\phi=0$. Bottom row, corresponding profiles across the horizontal midplane, exact (lighter/red) and toroidally averaged smoother curve (darker/blue). Times (a) $t=43$, (b) 126, (c) 227, (d) 462, and (e) 530. A central 1/1 island reduces central T_o and n_o.

metric perturbations that do not affect the mode). The perturbation rapidly consolidates nonlinearly to a characteristic filamentary helical shape with toroidal and poloidal localizations along the equilibrium field lines [cf. Figs. 7(a) and 7(b)]. Above a certain threshold amplitude, the volume averaged growth rate rises rapidly, Fig. 2 at $t \lesssim 40\tau_A$.

B. Off-midplane growth and ballooning outburst

As the harmonics consolidate, the instability begins to grow more strongly at some $\pm 60°$ off the midplane, Fig. 1(b) or Figs. 3 and 4 with midplane profiles. The off-midplane fingers appear to grow semi-independently, but are connected

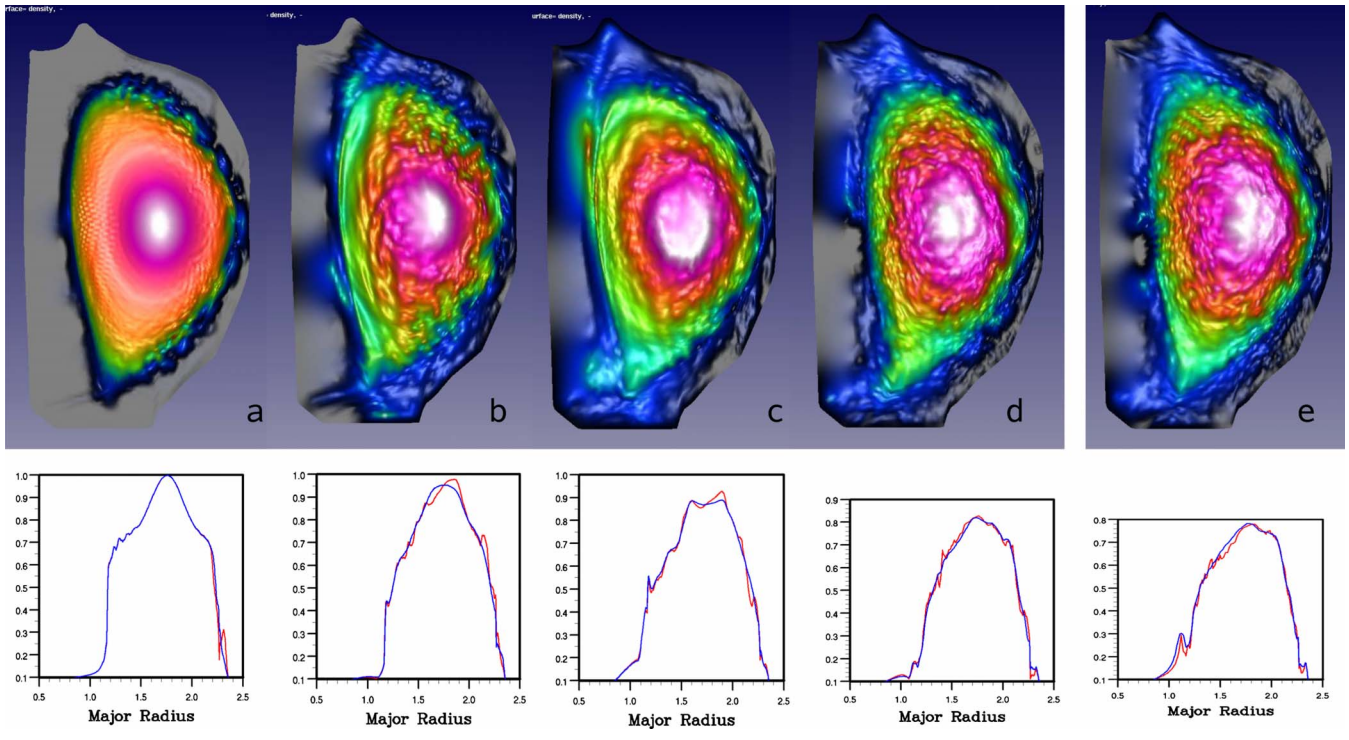

FIG. 4. (Color online) Density contours and profiles show greater anisotropy than temperature. Reference case, for the same times as Fig. 3.

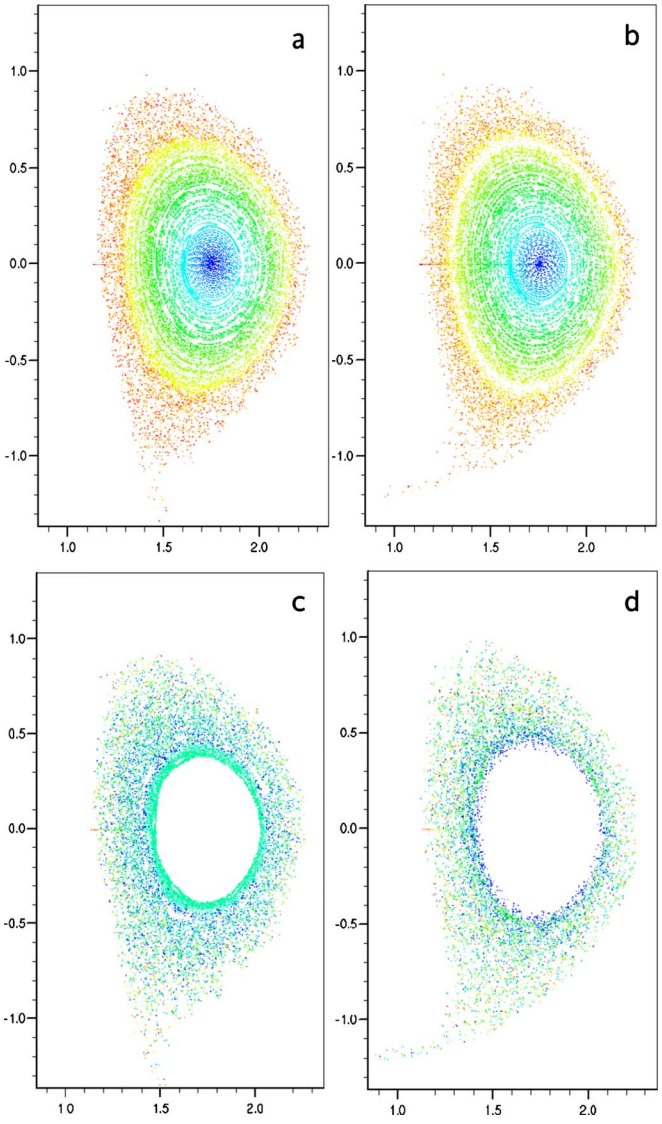

FIG. 5. (Color online) Magnetic puncture plots show asymptotic field splitting and tangle structure. Top $t=43$ and bottom $t=62$ for the reference case at $\phi=0$. Left plots [(a) and (c)] show field lines traced in the $+\phi$-direction (B_T), right [(b) and (d)] in $-\phi$, from the same starting points on the inner horizontal midplane. $t=43$ shows mostly good nested interior surfaces, with a narrow $m/n=1/1$ island. By $t=62$, the unstable tangle manifold loops have grown on the outboard edge. The interior, not shown, has good flux surfaces with a 1/1 island over $r/a<1/3$. The $+\phi$-direction has bigger loops near the bottom, $-\phi$ near the top.

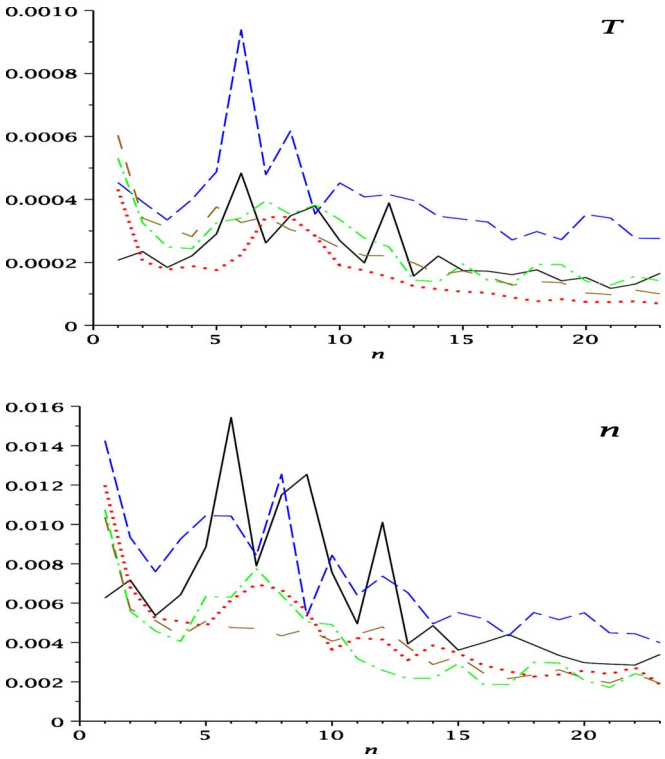

FIG. 6. (Color online) Nonaxisymmetric toroidal harmonics of temperature T and density for the reference case. Curves show times $t=43$ (solid line/black), 126 (dashes/blue), 227 (dotted-dashed/green), 461 (dots/red), and 604 (wide-spaced dashes/brown). Harmonics grow during the ELM crash and first inboard instability at $t=170-180$, then fall, except that $n=1$ remains high due to a 1/1 central island. Normalized L^2 norm over the volume inside the bounding wall, $(\int dx^3|f_n|^2/\int dx^3)^{1/2}$, plotted against the harmonic number. Equilibrium $n=0$ harmonics are large, $T_0=0.0211$ and $n_0=0.520$.

to the midplane along equilibrium field lines. Temperature and density fingers then rapidly burst outward over the entire outboard side, over some 20–30 μs [cf. Fig. 7(c)]. Temperature fingers are longer and more clearly defined than density. Equilibrium toroidal rotation increases the strength and definition of the outward fingers.

The local density gradient broadens rapidly on the outboard midplane, to well inside the original edge pedestal.[27,39] The edge temperature gradient is less affected. The volume-averaged exponential growth rate, defined from the square root of the kinetic energy integrated over the entire simulation domain, $[\int dx^3(nmv^2/2)]^{1/2}$, grows rapidly during the initial mode consolidation and the beginning of the ballooning burst to peak at $t\simeq 37$, then drops abruptly as the midplane ∇n weakens, although the plasma fingers continue to expand, as shown in Fig. 2.

As the ballooning burst saturates, the near-midplane plasma bulges shorten and smooth out. Outside the original LCFS, density concentrations or "blobs" shear off poloidally from the plasma, Fig. 1. Off the midplane, the lower density regions that alternate with the outgoing plasma fingers, also fingerlike, grow inward deeply into the plasma, apparently up to some bounding interior flux surface. (In 119690, the limit was $q\simeq 1$ as the central q_o dropped below unity and a 1/1 island formed.) Plasma is lost to the outboard side, first near the midplane, then to the off-midplane regions. A small inboard edge disturbance may also occur.

Few experimental observations of the off-midplane region exist. Alcator C-Mod sees large plasma fingers on the outboard side near the lower X-point.[52] Their angle, more vertical than transverse to the flux surfaces, resembles that of the simulation [e.g., Figs. 5(c) and 5(d) or Fig. 7(c), density].

C. Density loss to the divertor from near the X-points

In the second part of the ballooning outburst, starting at $t\simeq 72$, density fingers push out from near the X-points and detach into concentrated blobs outside the plasma, just outboard of the X-points. The lower blob moves promptly down into the adjacent outboard divertor, then drifts more slowly

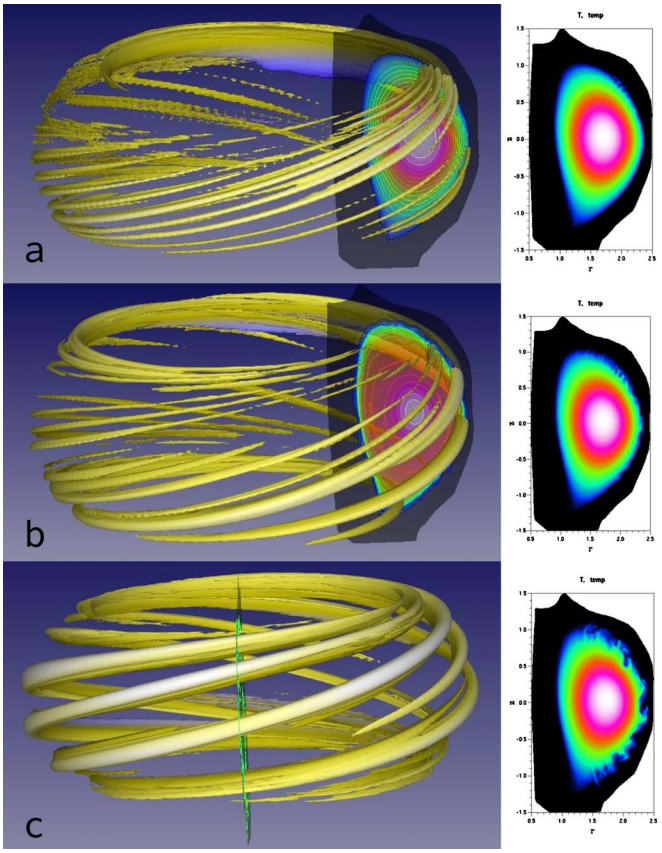

FIG. 7. (Color online) Nonlinear consolidation of harmonics leads to a helical filamentary plasma structure around the LCFS, shown by the perturbed poloidal magnetic flux $\tilde{\psi}$ (left frames). Times (a) $t=26$, (b) 40, and (c) 52, from small to large perturbation size (density contours shown at right). $\tilde{n}$ and $\tilde{T}$ have similar structure to $\tilde{\psi}$. High toroidal resolution ($n \leq 47$) two-fluid run of 119690 with no equilibrium toroidal rotation, initially perturbing all nonzero harmonics. Frame (c) is rotated 90° to show structure.

down and along the walls, staying outside of the outboard X-leg, Figs. 1(d) and 1(e). This wall contact is a likely source of the ejected deuterium atoms that produce the strong pulse of D-α emission in the divertor that characterizes the ELM. On the top of the plasma, a ridge of relatively cold density peels up and off toward the inboard side, Fig. 1(d). It connects to the upper divertor along the upper X-point outboard leg. A nearly vertical density ridge remains for over 140 μs, Figs. 1(e), 4(b), and 4(c). The remnants of the density are decaying in both divertors by around $t=227$, Fig. 4(c).

In contrast with the density ejection near the X-points, the temperature and pressure are expelled more evenly over the outboard side and flow along the helical unconfined field lines to the divertors, over a longer interval of several 10s of μs. After the initial ballooning, outboard finger growth may recur, but it never reaches the extent or strength of the primary outburst and remains within a small radial distance outside the original LCFS and poloidally closer to the midplane.

Experimental camera pictures of edge density blobs obtained from visible emission have approximate parameter dependences $n^{0.6}T^{0.5}$.[53] Time plots of this expression show stronger flow along the field lines than cross-field movement, quite similar to the pressure $p=nT$. The timing of the major initial divertor losses to the outboard then inboard sides, relative to the initial ballooning losses near the midplane, is similar to experimental observations,[7] although the proposed mechanism is different.

D. Stochastization of the magnetic field

The magnetic field stochasticizes from the plasma edge inward, following the inward growth of the low density and temperature fingers in the off-midplane region, Fig. 5 at $t=43$ and 62. Much of the stochasticity develops early, by $t \sim 100$, but the interior field continues to evolve, particularly on the inboard side.

Most field lines in the stochastic region mix radially over all or part of the affected region, although the absolute field perturbation is small, $|\tilde{\psi}|/|\psi_o| \lesssim 0.01$ in the poloidal flux. Most interior field lines are confined over many toroidal circuits, except those very near the original LCFS. Field lines are actually lost from near the X-points to the divertors. Many from the stochastic region are eventually lost to the lower divertor. Some are lost to the upper divertor.

The central plasma density loss is larger and faster than the temperature loss, consistent with experimental ELM and RMP observations. In 119690, the relatively large loss of central density and temperature results from growth of a central 1/1 magnetic island, as the initial $q_o \simeq 1$ drops below unity. The island is clearly seen in the puncture plots and in the temperature flattening in Fig. 3. Other ELMs, without internal modes, show little central loss.

There is little evidence of exterior field line loops connecting back into the plasma from the ballooning fingers, except from a short distance outside the original separatrix. Exterior field lines remain largely unconfined, similar to the equilibrium field. Other simulations[41] agree. This picture differs from flux-tube based models of plasma ballooning fingers.[54] In fact, many field lines lying just inside the original separatrix, but outside the higher density fingers, are rapidly lost through the X-points. This tends to create an annular region near the plasma edge that is only partially connected to the plasma interior, despite the radial excursions of interior field lines into this region.

E. Inboard edge instability

After the initial ballooning burst subsides, the outboard exterior region begins to clear of plasma. Quasiperiodic outboard disturbances may continue to expel plasma, but at a reduced level and the fingers never reach the extent of the original burst. The interior plasma instability and inboard magnetic tangle continue to develop, as suggested by the ripples in Figs. 1(d), 1(e), 3, and 4. Along the inboard edge, the density first develops one or two narrow ridges parallel to edge, similar to the expected loops of a homoclinic magnetic tangle. It then affects more interior regions around the midplane. Once this disturbance expands again to the inboard edge near the midplane, it triggers a strong edge instability. Two concentrations of cold plasma bulge outward, nearly symmetrically across the midplane, as in Fig. 4(e), which corresponds to the last growth rate spike in Fig. 2. The bulges separate and travel vertically up and down along the

plasma edge, e.g., Fig. 4(d), then Fig. 4(b). In the upper and lower divertors, density and temperature may partially accumulate near the inner magnetic X-leg, Figs. 3 and 4. Eventually they are lost to the walls. The temperature variation is smaller than for density in general.

For the steep, narrow edge pressure gradient of 119690, the inboard instability is strong and repetitive, as in Fig. 2. Before the first large inboard spike at $t \simeq 170$, the initial outboard instability has largely subsided and the outboard region begun to clear of plasma. [Similar, but smaller, inboard edge instabilities with limited plasma loss may occur earlier during the ballooning phase, Figs. 1(d) and 1(e).] A strong inboard instability may cause the lower X-point to temporarily elongate and curve inward, as in Fig. 4(d). More density is lost in a wider band along the inboard X-leg. The X-point displacement is limited and typically restores, Fig. 4(e).

In the National Spherical Torus Experiment (NSTX), periodic decreasing inboard-edge pulses of D-α light are regularly observed near the midplane, following the main outboard ELM loss. They are attributed to pulses of density lost from the inboard side midplane. NSTX also observes sequences of density blobs traveling down along the inboard plasma edge to the lower divertor in smaller ELMs (Ref. 55, Fig. 12). Most other plasma experiments do not measure the inboard side.

In experiments, the plasma and energy in the ELM filaments ejected in the outboard midplane region generally constitute only part of the total energy deposited on the divertors.[7] The simulation suggests that the difference may result from inboard losses, with some contribution from direct loss near the X-points on both sides.

F. Saturation and healing

The main ELM crash occurs before and during the two initial pulses of plasma to the outer and inner divertors. Over longer times, the outboard plasma boundary restores toward its original shape, including the X-point. In 119690, the outboard density boundary smooths by $t \simeq 184$. In other cases, such as 126006, the near-midplane region may later refill with additional local density from the plasma.

The interior magnetic field remains superficially stochastic at a low level beyond the simulation interval of several hundred microseconds. Nevertheless, the plasma interior relaxes toward axisymmetry, with small oscillations, as shown by the midplane profiles in Figs. 3 and 4 and the toroidal spectra in Fig. 6. Depending on the configuration, large scale, low-n and m interior structures may develop at longer times. In the 119690 case, a central, approximately 1/1 magnetic island grows and decays. At the actual resistivity, reconnection was incomplete, although complete sawtooth reconnection occurred at $S \leq 3.3 \times 10^6$. In 126006, $q > 1$ and another low-mode-number ($n=1,2,3$) structure developed at midradius. In the experiment[48] an $n=2$ structure developed after the toroidal rotation fell below a certain threshold.

The plasma in the divertors may continue to evolve over longer times, replenished by sporadic inboard instabilities. The divertor temperature has a roughly inverse distribution to the density.

G. Plasma rotation

Without equilibrium toroidal rotation, the initial outboard ballooning burst does not rotate in MHD, as expected theoretically. Poloidal rotation may develop, but no coherent toroidal rotation of the flux or density surfaces.

During the strong ballooning phase, oppositely directed flow vortices $\perp \hat{\phi}$ develop in the upper and lower halves of the plasma cross section. Starting as thin layers near the plasma edge, they expand to fill the upper and lower sections, over 1/3 to 1/2 of the minor radius from the X-points. The flow circulates outwards in R near the midplane, then around the plasma edge toward the local X-point, counterclockwise at the top, clockwise at bottom. In the divertor region, just inside and outside the LCFS, toroidal rotation develops quickly in the direction of the parallel motion driven by the vortices, counter-B_T in the upper divertor ($-\phi$ or into the page in Figs. 1, 3, and 4) and opposite in the lower divertor. This rotation is carried into the divertor region by the plasma. It persists well into the ELM healing phase, although it may be temporarily quenched by the arrival of inboard density blobs. At later times, the inboard plasma edge also tends to rotate toroidally in the counter-B_T direction.

Immediately after the initial outburst, the outboard plasma edge and detached blobs move poloidally, but their direction is not coherent. It initially tends to be counterclockwise (upward or in the electron diamagnetic direction for a downward ∇B drift). Partial or temporary direction reversals may occur variously in the upper and lower halves of the plasma, partly correlated with the periodic inboard instabilities that drive motion toward the X-points. Outside the plasma, density blobs move fairly coherently, but unsynchronized with the nearby plasma edge. Their direction also reverses in time.

At longer times, the plasma interior may develop a more coherent poloidal rotation. The rotation is exhibited more clearly by temperature contours than density. The source may be a poloidally asymmetric inboard/outboard flux surface pressure imbalance due to the X-point geometry[56] or particle diffusion,[57] at a rate that exceeds the damping due to magnetic pumping. In the simulations, the interior rotation at midradius eventually becomes clockwise, in the ion diamagnetic direction or upward on the outboard side. Once the interior rotation is well developed, it appears to enchain the plasma edge motion in the same direction.

Large low-n interior structures may grow and lock the poloidal rotation, as in case 126006. The plasma then bulged outward to contact the near-midplane walls.

Experiments observe a variety of poloidal motions for ELM filaments and density blobs, without a systematic explanation. The simulations suggest that the early motion is indeed fairly random and changes on fast time scales. Non-MHD effects may also be important.

IV. EARLY NONLINEAR MODE CONSOLIDATION

The early ELM instability develops a persistent, characteristic filamentary shape in MHD or two fluids, helically aligned along equilibrium field lines and localized to varying degrees in both toroidal and poloidal directions. The shape is consistent with a magnetic tangle.

The ELM trigger was not studied, since the simulation cases were initially unstable to MHD ballooning/peeling modes. Starting from a random disturbance of multiple toroidal harmonics, the perturbation grows in the steep gradient region on the outboard plasma edge, in the bad magnetic curvature region. As it begins to coalesce, but while the perturbation of the plasma boundary is still small, it tends to be largest around the midplane (in MHD) and radially mostly contained within the steep pedestal pressure gradient, similar to a ballooning-type eigenmode, as in Fig. 1(a), temperature.

In the reference case, nonlinear mode consolidation dominated over linear or quasilinear growth, as shown by the oscillating growth rate in Fig. 2 for $t<40\tau_A$. The rate and degree of consolidation depend on the plasma parameters, but strong nonlinear consolidation was also typical of other ELMs, even when the initial perturbation amplitude was greatly reduced.

Figure 7 illustrates the early nonlinear consolidation for a higher toroidal resolution run using $|n|\leq 47$ harmonics, twice the reference case. The case is two fluid[44] with the experimental strength $H=c/R\omega_{pi}=0.015$, but MHD behaves similarly. The structure develops earliest and most coherently in $\tilde{\psi}$, then $\tilde{T}$ and $\tilde{n}$. All three form similar high n and m ripples around the outboard side of the plasma, frame (a). The highest harmonics $n\simeq 40-44$ were prominent, consistent with the increasing growth rate with n of mostly ideal ballooning modes. (The reference case had $n\simeq 20-23$, again the maximum possible.) At both resolutions, the early instability rapidly consolidated [frames (b) and (c)] into a similar moderate $n=6-10$ perturbation with some $n=12$, modulated by a low-n envelope with $n=1-3$. The reference case spectra are shown in Fig. 6. The general banded helical shape, slightly smoothed, persists for long times.

The nonlinear perturbation resembles the localized bands or "filaments" of light emission aligned along equilibrium field lines that are seen in DIII-D[58–60] and many other experiments.[61–65] Unfortunately, no experimental pictures exist for the simulated cases. The lower harmonics of the consolidated instability match the observed filaments better than the higher harmonics predicted by single-mode MHD growth rates. The poloidal magnetic flux $\tilde{\psi}$ typically develops the cleanest helical structure early and suggests the possibility of a clear magnetic signal early in the ELM crash.

V. DISCUSSION: MAGNETIC TANGLE

A. Equilibrium magnetic field

The equilibrium magnetic field configuration strongly influences the ELM. In the early stages, it determines where and how the asymptotic field splitting is most easily produced. Ballooning modes are strongly aligned to the magnetic field and the perturbed field lines remain locally mostly aligned to the equilibrium field lines, even as the flux surfaces break up and the field lines mix radially due to the ELM. This allows other, more slowly growing instabilities that depend on the equilibrium configuration to develop eventually.

For DIII-D plasmas with $q_{95}\simeq 3.5$, field lines over most of the outboard side wrap approximately once toroidally as they move from the top to bottom of their flux surface, as shown by the essentially field-line-following perturbations in Fig. 7. In a spherical torus at higher q_{95}, outboard field lines have a more vertical pitch and cover a smaller fraction of the toroidal circumference between top and bottom, e.g., half or one-third in NSTX. Tighter toroidal winding near the top and bottom completes a full circuit, while extra toroidal winding occurs on the inboard side. In addition, near the X-points field lines wrap many times at the top and bottom, almost toroidally. The mostly toroidal region may extend over a surprisingly wide minor radius at the top and bottom of the plasma, compared to the narrow flux surface separation on the outer midplane. The dense toroidal winding makes it easy to grow field loops almost vertically inward in these regions.

The unconfined field lines on the outboard side also wrap approximately once toroidally over the plasma height, except very near the wall, where they may hit the wall. Above and below the plasma, they may wrap a few additional times, mostly toroidally, before hitting the walls. On the inboard side, the unconfined field lines again approximately follow the confined near-edge field lines, wrapping a similar number of times between top and bottom.

D-shaped plasmas thus have relatively little radial shear over their outboard side, from $q\simeq 1$ to well outside the plasma near the wall. This gives ballooning modes a coherent helical structure even at large amplitude and strengthens the parallel coupling between the top and bottom of the plasma.

B. Homoclinic-like tangle

The instantaneous toroidal magnetic field forms a Hamiltonian system with two degrees of freedom,[11] whose mathematical theory is comparatively simple and well developed.[12,13] The ELM magnetic field exhibits many of the features of a theoretical homoclinic tangle due to a single X-point. It also experiences some heteroclinic tangle effects due to the detached upper X-point, as also observed in RMP studies.[66]

The ELM tangle differs from the ideal Hamiltonian form when its time evolution is considered. The ideal theory is valid for sufficiently small perturbations, but produces infinitely large disturbances over infinitely fine scales. The actual plasma response is finite, limited by the MHD times and other plasma processes. In the simulation, it is also limited by the finite resolution of the spatial grid.

The discrepancy is crucial to the ELM. A Hamiltonian system preserves phase space volume, so that the unstable field loops should have equal areas on each side of the original separatrix. Instead, the external ELM magnetic loops have very limited extent, while the internal loops can grow

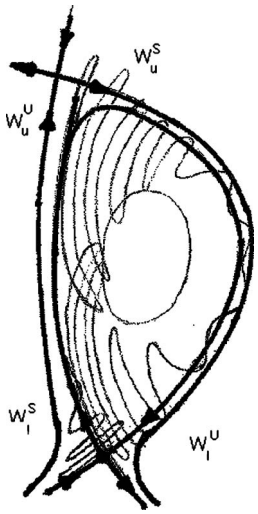

FIG. 8. Schematic interpretation of the magnetic tangle at times $t \gtrsim 100$, in a constant-ϕ cross section. Thick curves show equilibrium stable and unstable (superscript) manifolds $W_{u,l}^{S,U}$ of the upper and lower X-points (subscripts); arrows show the direction of successive field line intersections. Thin lines show the perturbed "unstable" manifold loops (W_u^U not shown) and a central bounding flux surface. Orientation is for a DIII-D plasma with B_T clockwise viewed from top of torus and I_p opposite.

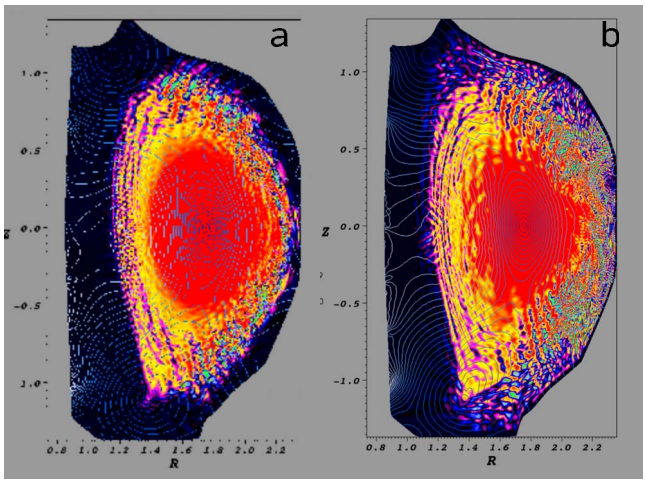

FIG. 9. (Color online) Toroidal current density ($-RJ_\phi$) variation as a marker for magnetic reconnection suggests interchange, rather than magnetic tearing. (a) $t=43$ at the beginning of the ballooning outburst. (b) $t=136$ as ballooning subsides, but inboard tangle develops. Coloring emphasizes a restricted range around zero. Light color (yellow online) and medium color central core (red online) denote positive values. Dark narrow lines (blue online) in the lighter areas are negative. Black is zero current, including the exterior vacuum. Background curves show equispaced contours of $|B_{\perp\phi}|$.

deeply inward and continue to evolve after the outboard ballooning saturates, leading to the inboard edge instability.

Near-Hamiltonian asymptotic surface splitting is a special case of the much more general splitting of invariant manifolds, not necessarily Hamiltonian. For the plasma dynamics at higher dimension, ideal MHD has Hamiltonian formulations[67,68] that allow the possibility of equilibrium solutions that are invariant manifolds. Resistive or extended MHD are not Hamiltonian. Resistivity or an equivalent process is crucial for the tangle, by allowing changes from a "frozen-in" axisymmetric equilibrium field. The simulations strongly suggest that field splitting of a freely moving plasma magnetic boundary is a robust process in extended MHD and may not even require primary X-points directly on the boundary, merely sufficiently close.

A schematic interpretation of the nonlinear ELM magnetic tangle is shown in Fig. 8. Since the tangle is defined only by its asymptotic limits, it is difficult to extract directly from a nonlinear state and the figure represents an interpretation. The inboard and near-X-point loops are drawn wider than actual, for clarity, cf. Figs. 1 and 9. In 3D, the loops form helical lobes, similar to Fig. 7.

The figure shows the well-developed nonlinear stage immediately after the ballooning burst, but before the inboard instability is triggered, $t \simeq 100-160$ in the reference case. At earlier times, narrow unstable loops originating from ballooning unstable region just outboard of the X-points grow around the plasma interior parallel to the inboard edge, from both top and bottom. They align closely along the height of the inboard edge, as suggested (and exaggerated) by the ripples in J_ϕ in Fig. 9(a). The oppositely growing loops interact to create refraction patterns on the inboard side. Unlike the classic homoclinic/heteroclinic tangle, these spread and appear to curve inward near the midplane.

The thick lines represent axisymmetric equilibrium flux surfaces. Arrows indicate the direction of successive intersections of a field line. The segments connecting to the X-points form the equilibrium stable and unstable manifolds $W_{u,l}^{S,U}$ for the upper and lower X-points, as labeled. The thin lines show the perturbed unstable manifold loops. On the outboard side, the unstable manifold of the lower X-point follows the lower fingers as a field line approaches the X-point. The unstable manifold of the upper X-point (coincident with the stable manifold of the lower X-point) follows the above-midplane loops that approach the top of the plasma. The stable perturbed manifolds, defined by field lines traced away from the X-point, remain close to the original surfaces. Similar stable and unstable manifolds exist on the inboard side of each X-point. The unstable manifolds on the inboard side generally have smaller excursions, but may grow temporarily during the later ELM, as suggested by Fig. 4(d).

C. Interchange instability

The toroidal current density J_ϕ, Fig. 9, interpreted as a marker for potential magnetic reconnection, displays signatures characteristic of interchange instabilities, rather than magnetic islands produced by tearing modes, particularly near the X-points. Near the top and bottom of the plasma, the contours align to form nearly vertical fingers pointing radially into the plasma. Magnetic tearing would require progressive helical resonances and breakdown of nested toroidal flux surfaces into magnetic islands of increasingly fine scale. The strong radial current alignment, persisting throughout the tangle field penetration stage, would be difficult to produce from the current extrema located at the X- and O-points of magnetic islands, across rational surfaces of continuously varying safety factor q. It is consistent with tangle loops formed by interchange, whose shape depends on the equilib-

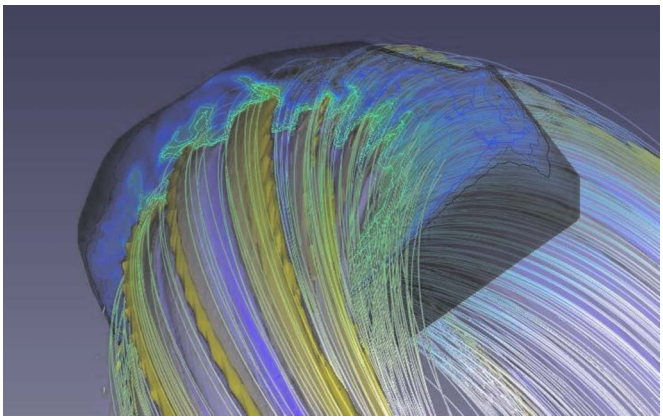

FIG. 10. (Color online) Surface of constant temperature located inside the plasma, colored according to values of the poloidal magnetic flux ψ, representing minor radius, and a single magnetic field line started near the surface and traced in the lower X-point unstable (B_T) direction. The cut plane shows equispaced temperature contours. Tilted up to show the bottom of the plasma. Rotating 119690 case with reference parameters, except $n_{vac}=0.2n_o$.

rium topology of the X-point and adjacent surfaces. Other plasma variables, including the velocity poloidal stream function u, suggest similar radial alignment and have an interchange, rather than tearing, parity.

The lack of islands also fits the expected effect of a Hamiltonian tangle on nested interior surfaces in phase space. The equilibrium flux surfaces affected by the tangle break down almost immediately to chaos,[14,17] including the residual KAM surfaces. The depth of the current density variation approximately matches that of the stochastic field region, Fig. 5, which is slightly wider than the macroscopic disturbance in density and temperature.

Field line tracing and magnetic puncture plots also support a general lack of island structure. The puncture plots show the characteristic appearance of near-Hamiltonian chaos, with structures resembling 3D voids or bubbles rather than islands, Fig. 5.

D. Magnetic structure

Despite its superficial stochasticity, the magnetic field possesses overall structure. First, it generally follows the plasma perturbation in n and T, or p. Second, locally the field lines remain generally aligned with the axisymmetric equilibrium field. Most interior field lines are confined for many toroidal transits. A central core is almost completely confined. Outside this radius, many field lines have radial excursions and are eventually lost from the vicinity of the X-points to the divertors. For a single lower X-point, more are lost to the bottom divertor.

Figure 10 shows that a single field line approximately follows a single constant temperature contour over many toroidal transits and the general T contours over longer intervals. The shadowing is not exact. The line was finally lost from near the X-point. This 119690 case had equilibrium toroidal rotation and $S=3.3\times10^6$, but the behavior is a general property and was similar in all cases. (While the simulation may not always accurately follow a single field line, the line actually traced represents a good approximation to substantial pieces of real field lines.)[13]

Partial confinement of some field lines within annular flux volumes, rather than flux surfaces, may be seen relatively early in the ELM. Different field lines have differing degrees of excursion, as suggested in Fig. 5 (online), where nearby starting points lying on the inboard midplane have similar color. Many individual field lines, particularly near the plasma edge, remain confined within a relatively narrow annulus of the edge for long distances, until lost from the plasma.

Faster loss of density than temperature, observed in both ELM and RMP simulations[27,39] when the temperature equilibrates along field lines much faster than the density, and in many experiments, argues against a completely mixed stochastic field. The containment of field lines for many toroidal transits, before localized loss from small areas near the X-points, may help preserve the temperature gradient by mixing the temperature over a range of minor radii in both directions during many toroidal circuits and also averaging over the excursions of many individual field lines. The density crosses field lines more directly by perpendicular diffusion, without a compensating parallel mixing. Magnetic braiding[69] of multiple overlapping islands predicts poorer confinement of temperature than density, the opposite of the simulation.

Evidence for preservation of the equilibrium field structure also appears in the longer time behavior. The total poloidal flux is only weakly perturbed. Over several hundred Alfvén times, equivalent to a few hundred microseconds in the DIII-D 119690 reference case, the plasma density and temperature smooth back toward their toroidal averages over most of the plasma, Figs. 3 and 4, despite continuing periodic edge disturbances. The higher toroidal harmonics decay from their initial maxima, Fig. 6. An $n=1$ component remains, due to the central 1/1 island, but it is much smaller than the axisymmetric piece. The plasma shape returns toward the original boundary, although the magnetic field remains chaotic at a low level.

At intermediate times, well after the initial ballooning subsides, large low-n structures can develop in the plasma interior. In 126006, with q strictly above unity, a large midradius structure with significant $n=2$ developed that caused the plasma to bulge out near the midplane to the wall. It locked the poloidal rotation. In the experiment,[48] an $n=2$ structure grew when the toroidal rotation was deliberately reduced to a critical level. It eventually locked to the wall and caused an H to L transition. The core MHD activity was correlated with D-α emission in the lower outer divertor, consistent with plasma loss to the outboard side.

E. Inboard edge losses

In most experiments the inboard plasma edge is MHD stable, but ELM plasma loss is often observed from the inboard side. The magnetic tangle provides a natural mechanism for outboard ballooning to drive a delayed inboard edge

TABLE I. Scaling with resistivity.

S	$t(\tau_A)$	γ	$\lvert\tilde{\psi}\rvert_m$	$\lvert\tilde{n}\rvert_m$	$\lvert\tilde{n}\rvert$ range	n_o
3.3×10^5	21.5	−0.0105	5.1×10^{-6}	0.0051	0.10/−0.11	1.00
3.3×10^6	21.5	−0.0106	4.4×10^{-5}	0.106	0.15/−0.16	1.00
3.3×10^7	21.5	−0.0101	8.0×10^{-5}	0.092	0.16/−0.19	1.00
3.3×10^5	42.8	0.0787	2.4×10^{-4}	0.34	0.31/−0.37	1.00
3.3×10^6	42.8	0.0779	3.56×10^{-4}	0.30	0.35/−0.33	1.00
3.3×10^7	42.8	0.0418	5.2×10^{-4}	0.32	0.34/−0.22	1.00
3.3×10^5	64.1	0.0356	6.35×10^{-4}	0.40	0.48/−0.42	0.99
3.3×10^6	64.1	0.0354	1.12×10^{-3}	0.33	0.39/−0.45	0.99
3.3×10^7	62.3	0.0120	9.4×10^{-4}	0.33	0.35/−0.37	1.00
3.3×10^6	101.2	−0.00341	0.00170	0.325	0.44/−0.33	0.98
3.3×10^7	104.6	0.00440	0.00147	0.37	0.41/−0.35	0.99

instability. The simulations show that the inboard side can potentially play an important role in ELM density and power losses.

The time delay for the first large inboard edge instability, after the outboard ballooning burst, some 100 μs in the reference case, is similar to that observed in experiments, roughly an ion transit time from outboard to inboard along equilibrium field lines around the plasma edge at the ion sound speed. The mechanism, however, depends on the tangle development and does not require plasma motion directly along field lines.

The wide inboard vacuum region in the 119690 reference case allowed the density and temperature to spread slightly beyond the true wall distance before being limited by dissipation. The inboard behavior was qualitatively similar to the 126006 case using the exact plasma-wall separation. There, the inboard density blobs could extend nearly onto the wall. The simulations also indicate that temporary density concentrations could form in the inboard SOL just outside the plasma. Some were nearly axisymmetric rings, while others had toroidal gaps. The rings remain for varying periods before moving up or down the center stack, in some cases apparently being swept out by the inboard edge activity.

VI. DISCUSSION: GROWTH RATES

A. Scaling with resistivity

Asymptotic magnetic field splitting requires breaking the ideal MHD constraint in order to change the direction of the field lines. The low values of resistivity typical of fusion plasmas suffice for magnetic reconnection, i.e., slippage of field through the plasma, to redirect the field lines locally over microscales. Although the midsection and top of the edge pedestal, where much of the ELM action takes place, are only weakly resistive, scans show that the ELM growth is partly resistive down to low values of the central plasma resistivity.

Resistivity increases the growth rate of linearized ballooning/peeling modes that are near or beyond ideal MHD instability.[70] It also increases the early nonlinear ELM growth. Table I compares the results for MHD, for the reference case 119690 at the actual peak plasma resistivity, Lundquist number $S=3.3\times10^7$, and two higher resistivities, $S=3.3\times10^6$ and 3.3×10^5. Due to the complex structure of the multiharmonic ELM, it is difficult to define a universal growth rate. The table shows several local and global parameters. The volume averaged growth rate γ is based on the square root of the kinetic energy integrated over the plasma plus vacuum, as in Fig. 2. Negative values at $t=21.5$, when the perturbation is small and confined to a narrow layer near the plasma edge, reflect the beating of toroidal harmonics.

The other parameters in the table measure changes on the outboard side of the plasma. The perturbed poloidal magnetic flux is shown by its maximum magnitude $\lvert\tilde{\psi}\rvert_m$ near the midplane (subscript m), within an angle $\pm10°$ measured from the magnetic axis. It shows rapid initial growth over the edge pedestal region. Its growth after $t=64$ reflects magnetic changes deeper inside the plasma. The total ψ remains nearly axisymmetric and little changed, with equilibrium value $\lvert\psi_o\rvert=0.02$ on the magnetic axis and near zero at the separatrix. In contrast, the maximum perturbed density near the midplane $\lvert\tilde{n}\rvert_m$ quickly saturates in the edge region at approximately 1/3 the central peak value $n_o=1.0$, showing the rapid saturation of the initial ballooning on the midplane as the local density gradient weakens. (The original pedestal top $n_p\simeq0.7$.) The perturbed density over the outboard pedestal continues to grow, shown by the extremal values in $\lvert\tilde{n}\rvert$ range, reflecting near-edge changes well off the midplane, including the large fingers.

Lower resistivity reduces the outward ballooning. The expelled density remains closer to the LCFS and more localized poloidally near the midplane and within the top and bottom finger regions. The poloidal spacing of the temperature and density fingers near the top and bottom of the plasma varies, not always consistently toward finer structure. Lower resistivity and viscosity also reduce the strongly backward curling mushroom shapes of the plasma fingers pro-

duced by flow vortices that resemble the classical Rayleigh–Taylor fluid instability. The new shape more closely resembles experimental density blobs.

The penetration of the lower density and temperature fingers into the core is less affected by resistivity. The rate of inward growth of the plasma fingers and central plasma loss slows at lower resistivity, but the penetration depth remains similar over a factor of 100 in S, up to at least $S \geq 3.3 \times 10^5$. The limit appears to be a low rational number flux surface determined by the plasma configuration. In 119690, where $q_o < 1$, it extended to $q=1$. A complete $m/n=1/1$ central sawtooth crash was observed at $S \leq 3.3 \times 10^6$, but only partial reconnection at $S=3.3 \times 10^7$.

Most H-mode fusion plasmas rotate toroidally. The DIII-D cases also had significant rotation very near the plasma edge.[71] Simulation indicates that, for strongly unstable ELMs, rotation increases the size of the outward ballooning fingers during the initial outburst, in radial extension and somewhat in poloidal width. At $S=3.3 \times 10^7$, the increased amplitude was very roughly equivalent to a factor of 10 times increase in resistivity. Similar to resistivity, rotation had little effect on the final inner extent of the instability. It also had little effect on the interior 1/1 mode in 119690, consistent with the observation of sawteeth in the actual experiment.[47]

B. Field splitting and magnetic tangle effects

In the absence of a freely moving plasma boundary, MHD theory encounters difficulties in explaining ELM stability, even when X-points are included. Many H-mode edge gradients are unstable to ideal MHD ballooning or peeling eigenmodes localized within the edge pressure pedestal, when no ELMs appear in experiment. The corresponding resistive modes are even more unstable. A large body of comparisons[35] shows that the ideal MHD growth rate of single toroidal harmonic modes must be systematically reduced to match the ELM onset. One method[35] subtracts the ion diamagnetic drift, $\gamma = \gamma_{\mathrm{MHD}} - (1/2)\omega_{*i}$, where the drift frequency $\omega_{*i}=k_\theta v_{*i}$ contains a poloidal wavenumber $k_\theta = m/r$ that can be large for high toroidal mode numbers n, since $m \simeq q_{95} n$. The factor 1/2 is imprecise, since γ_{MHD} varies rapidly near marginal stability. Furthermore, ion diamagnetic stabilization is theoretically incomplete. The present simulations using a diamagnetic two-fluid model[44] show that ion diamagnetic effects are relatively weak for realistic two-fluid strengths, for the moderate toroidal harmonics of the nonlinearly consolidated instability.

Linearized perturbation theory[31] assumes a coherent perturbation of the entire magnetic field, based on the assumption of well-defined flux tubes. The perturbed field behaves the same in both directions. The free boundary plasma should behave similarly as long as the boundary is not perturbed. At any level of boundary perturbation, however, asymptotic field splitting occurs. Only the unstable half of the split field can move with a transverse plasma displacement. The stable half remains close to the unperturbed field and acts as a drag on the plasma motion. These manifolds represent only asymptotic limits, but combined with their intermediate connecting field lines, should still exert extra drag compared to the linearized theory.

To test these effects, the magnetic field can be artificially constrained near the X-points. Experimental tests show effects, but they are difficult to separate from independent changes in the pedestal, since increased wall coupling tends to reduce edge pressure gradients. The JET experiment has had several divertor configurations. Before 1994, the lower X-point was close to the bottom wall and it saw mostly smaller type III ELMs.[9] In 1994, the plasma was raised and divertor pumps installed. The new plasma saw mostly large type I ELMs, but the plasma shape and other factors changed. From 1999 to 2001, a triangular "septum"[72] was installed between the X-legs, with the gas box divertor. The top of the septum, a broad rounded dome, stuck up far enough to contact the plasma to varying degrees. ELMs occurred at reduced size and frequency, but again the plasma edge changed.

Rigidly fixing the plasma boundary removes the field splitting, but also removes the free boundary effects on the linearized mode, i.e., the surface energy term in δW due to the boundary motion. In the simulation, the method of constructing and packing the spatial grid and the fact that the plasma equilibrium makes small initial adjustments to the grid prevented the separatrix from being fixed exactly.

Removing the X-point by smoothing the boundary shape changes essential features of the magnetic configuration, i.e., the close spacing of the field lines on a flux surface as they approach the top and bottom of the plasma. Exterior stability effects also change, since the adjacent flux surfaces become closed surfaces defined by wrapped field lines, which are stable in the Hamiltonian perturbation analysis.

Close walls can also disrupt the continuity of the unstable manifold loops that define the tangle structure. Field lines hitting a wall can move more independently than field lines tied into the plasma on both ends. The test therefore moved the domain walls close to the plasma, in two steps. First, the upper X-point was cut off by placing a planar horizontal wall above the plasma, at 20% of the distance between the plasma and the original uppermost wall point (just below $Z=1.0$ in Figs. 5 or 9). The magnetic field on the wall matched the equilibrium field there. In the second step, a horizontal planar surface was placed just below the lower X-point, at 1% of the original wall-to-plasma distance. The original field at the wall location was again preserved. In both cases, the linearized perturbation remains identical to the original.

Results are shown in Table II for the reference 11 960 case of Table I at $S=3.3 \times 10^7$. (Small differences in the models give slightly different numbers, but the mode remains very similar.)

Removing the upper X-point ("top wall") significantly accelerates the early nonlinear instability. The initial ballooning instability grows much faster from small size to ballooning outburst. At a given time, the plasma fingers extend further toward the wall, particularly off the midplane. The generic shape is similar, but the fingers are generally wider poloidally, with less fine structure near the top and bottom of

TABLE II. Constrained boundary.

Shape	$t(\tau_A)$	γ	$\|\tilde{\psi}\|_m$	$\|\tilde{n}\|_m$	$\|\tilde{n}\|$ range	n_o
Original	21.47	−0.0100	8.0×10^{-5}	0.092	0.16/−0.19	1.00
Top-wall	21.50	0.0765	2.46×10^{-4}	0.256	0.27/−0.28	1.00
Two-wall	21.50	0.0240	2.17×10^{-4}	0.260	0.27/−0.24	1.00
Original	42.82	0.0415	5.20×10^{-4}	0.328	0.33/−0.37	1.00
Top-wall	42.80	0.0186	1.35×10^{-3}	0.370	0.39/−0.36	1.00
Two-wall	40.39	0.00893	8.42×10^{-4}	0.367	0.39/−0.46	1.00

the plasma. The fingers in the lower half of the plasma increase in size and shape similarly to the upper half. These effects are consistent with the removal of a constraint on the outboard magnetic tangle. The unstable field lines are no longer confined by the equilibrium field line spacing along the upper X-point surface and the loops can change width to better match the midplane-driven instability. Due to the continuity of the tangle field lines around the separatrix, the lower loops are also less confined.

Disconnecting the lower unstable outboard manifold loops ("two-wall") has only a small effect, in the opposite direction to the top wall. Due to the shape of the plasma boundary and wall, the loops are cut off only very near the X-point, providing a small localized effect. The effect of removing the upper X-point dominates and the early instability looks similar to the top-wall alone. As in Table I, the average growth rate is a poor guide to the amplitude during the early consolidation phase at $t=21.5$. The final time shown, $t=40.4$, is earlier than the other cases, due to numerical problems in the strongly nonlinear stage. The grid points below the plasma were squeezed between the X-point and the wall and shortly after this time, numerical resolution was lost.

Thus, asymptotic field splitting and the resulting magnetic tangle act as a constraining force on the initial outward ballooning phase of the ELM. The effect is consistent with experimentally observed ELM stability trends.

VII. CONCLUSIONS

Numerical simulation of ELMs in H-mode plasmas in the DIII-D tokamak has been carried out with extended MHD models in the M3D code, at realistic and near-realistic resistivity. The results show that ELMs in toroidally confined fusion plasmas represent a new class of nonlinear plasma instability, where the plasma motion couples to part of a stochastic magnetic field. The resulting multistage ELM has many features similar to experimental observations in a number of machines. Losses to the divertor can occur directly from near the X-points on both outboard and inboard sides.

In a toroidal plasma, a freely moving magnetic boundary surface that contains one or more X-points behaves similarly to a Hamiltonian dynamical system with two degrees of freedom. As an unstable ballooning or peeling mode grows in the steep pressure gradient near the plasma edge, the plasma separatrix is perturbed and the magnetic surface splits into two, defined asymptotically by the limiting locations of the field lines when traced infinitely in opposite directions. The unstable surface, defined by the field lines approaching the X-point, develops large oscillations around the original boundary. The stable surface remains near the original. The intersection of these surfaces forms a chaotic magnetic tangle. The actual tangle is non-Hamiltonian, but retains many similarities to the idealized case.

Multiple toroidal harmonics consolidate nonlinearly at low amplitude to produce a moderate mode number ballooning instability. Outward-ballooning plasma fingers develop rapidly well off the midplane. An initial fast ballooning outburst occurs simultaneously over most of the outboard side. Near the X-points, the lower density fingers propagate deeply into the plasma core via a field-aligned interchange process, together with the magnetic tangle loops. Interior magnetic flux surfaces are destroyed without extensive resonant magnetic island formation. Many field lines mix over significant radial distances and many are eventually lost from the X-point regions.

The tangle couples the outboard to the inboard plasma edge. An inboard edge instability can develop and produce significant plasma loss. The plasma eventually relaxes back toward the original axisymmetric configuration. It may have decaying, quasiperiodic pulses of edge activity.

A partly stochastic instability offers a potential explanation for the large variety of ELM and ELM-free behavior observed experimentally in H-mode plasmas. The stable half of the field and the constrained form of the unstable loops approaching the X-points provide a drag on the early instability that may help explain why ideal MHD linearized perturbation theory alone generally predicts excess instability. Plasma edge instabilities provide a natural mechanism for creating and sustaining low levels of magnetic stochasticity in the plasma edge that could explain the steep edge pressure gradient of the H-mode and its requirement for a minimum level of plasma heating.

ACKNOWLEDGMENTS

The authors thank Todd Evans for suggesting homoclinic tangle fields and the DIII-D experiment at General Atomics, San Diego, for permission to use experimental data. Thanks also to Janet Jacobsen of LBL NERSC and David Pugmire of ORNL NCCS for help with visualization.

This work was supported by the U.S. Department of Energy Office of Fusion Energy Sciences Theory and SCiDAC programs. Simulations were run on the Cray XT-4 and visu-

alization server at the National Energy Research Scientific Computing Center, supported by the Office of Science of the U.S. Department of Energy Contract No. DE-AC02-05CH11231.

[1]F. Wagner, G. Becker, K. Behringer, D. Campbell, A. Eberhagen, W. Engelhardt, G. Fussmann, O. Gehre, J. Gernhardt, G. v. Gierke, G. Haas, M. Huang, F. Karger, M. Keilhacker O. Klüber, M. Kornherr, K. Lackner, G. Lisitano, G. G. Lister, H. M. Mayer, D. Meisel, E. R. Müller, H. Murmann, H. Niedermeyer, W. Poschenrieder, H. Rapp, H. Röhr, F. Schneider, G. Siller, E. Speth, A. Stäbler, K. H. Steuer, G. Venus, O. Vollmer, and Z. Yü, Phys. Rev. Lett. **49**, 1408 (1982).
[2]B. Coppi, Phys. Rev. Lett. **39**, 939 (1977); J. W. Connor, R. J. Hastie, and J. B. Taylor, *ibid.* **40**, 396 (1978).
[3]D. Lortz, Nucl. Fusion **15**, 49 (1975).
[4]J. A. Wesson, Nucl. Fusion **18**, 97 (1978).
[5]M. Keilhacker, G. Becker, K. Bernhardi, A. Eberhagen, M. ElShaer G. Fussmann, O. Gehre, J. Gernhardt, G. V. Gierke, E. Glock, G. Haas, F. Karger, S. Kissel, O. Kluber, K. Kornherr, K. Lackner, G. Lisitano, G. G. Lister, J. Massig, H. M. Mayer, K. McCormick, D. Meisel, E. Meservey, E. R. Muller, H. Murmann, H. Niedermeyer, W. Poschenrieder, H. Rapp, B. Richter, H. Rohr, F. Ryter, F. Schneider, S. Siller, P. Smeulders, F. Soldner, E. Speth, A. Stabler, K. Steinmetz, K.-H. Steuer, Z. Szymanski, G. Venus, O. Vollmer, and F. Wagner, Plasma Phys. Controlled Fusion **26**, 49 (1984).
[6]S. M. Kaye, M. G. Bell, K. Bol, D. Boyd, K. Brau, D. Buchenauer, R. Budny, A. Cavallo, P. Couture, T. Crowley, D. S. Darrow, H. Eubank, R. J. Fonck, R. Goldston, B. Grek, K. P. Jaehnig, D. Johnson, R. Kaita, H. Kugel, B. Leblanc, J. Manickam, D. Manos, D. Mansfield, E. Mazzucato, R. McCann, D. McCune, K. McGuire, D. Mueller, A. Murdock, M. Okabayashi, K. Okano, D. K. Owens, D. E. Post, M. Reusch, G. L. Schmidt, S. Sesnic, R. Slusher, S. Suckewer, C. Surko, H. Takahashi, F. Tenney, H. Towner, and J. Valley, J. Nucl. Mater. **121**, 115 (1984).
[7]A. W. Leonard, N. Asakura, J. A. Boedo, M. Becoulet, G. F. Counsell, T. Eich, W. Fundamenski, A. Herrmann, L. D. Horton, Y. Kamada, A. Kirk, B. Kurzan, A. Loarte, J. Neuhauser, I. Nunes, N. Oyama, R. A. Pitts, G. Saibene, C. Silva, P. B. Snyder, H. Urano, M. R. Wade, and H. R. Wilson, Plasma Phys. Controlled Fusion **48**, A149 (2006).
[8]G. T. A. Huysmans, Plasma Phys. Controlled Fusion **47**, B165 (2005).
[9]H. Zohm, Plasma Phys. Controlled Fusion **38**, 105 (1996).
[10]K. Ikeda, Nucl. Fusion **47**, S1 (2007); ITER Physics Expert Group on Divertor, ITER Physics Expert Group on Divertor Modelling and Database, and ITER Physics Basis Editors, *ibid.* **39**, 2391 (1999).
[11]A. H. Boozer, Phys. Fluids **25**, 520 (1982); **26**, 1288 (1983).
[12]J. Guckenheimer and P. J. Holmes, *Nonlinear Oscillations, Dynamical Systems, and Bifurcations of Vector Fields* (Springer-Verlag, New York, 1983).
[13]A. J. Lichtenberg and M. A. Lieberman, *Regular and Chaotic Dynamics*, 2nd ed. (Springer-Verlag, New York, NY, 1992), discussed in many texts on Hamiltonian dynamics.
[14]V. I. Arnold, V. Kozlov, and A. I. Neishtadt, *Mathematical Aspects of Classical and Celestial Mechanics*, 3rd ed. (Springer, New York, 2006) and earlier editions, transl. E. Khukhro.
[15]R. K. W. Roeder, B. I. Rapoport, and T. W. Evans, Phys. Plasmas **10**, 3796 (2003).
[16]T. E. Evans, R. K. W. Roeder, J. A. Carter, B. I. Rapoport, M. E. Fenstermacher, and C. J. Lasnier, J. Phys.: Conf. Ser. **7**, 174 (2005).
[17]A. J. Dragt and J. M. Finn, J. Geophys. Res. **81** 2327, doi:10.1029/JA081i013p02327 (1976); J. Math. Phys. **20**, 2649 (1979).
[18]H. Poincaré, *Les Methodes Nouvelles de la Mechanique Celeste* (Gauthier-Villars, Paris, 1892).
[19]T. E. Evans, R. A. Moyer, P. R. Thomas, J. G. Watkins, T. H. Osborne, J. A. Boedo, E. J. Doyle, M. E. Fenstermacher, K. H. Finken, R. J. Groebner, M. Groth, J. H. Harris, R. J. La Haye, C. J. Lasnier, S. Masuzaki, N. Ohyabu, D. G. Pretty, T. L. Rhodes, H. Reimerdes, D. L. Rudakov, M. J. Schaffer, G. Wang, and L. Zeng, Phys. Rev. Lett. **92**, 235003 (2004).
[20]T. E. Evans, I. Joseph, R. A. Moyer, M. E. Fenstermacher, C. J. Lasnier, and L. W. Yan, J. Nucl. Mater. **363–365**, 570 (2007).
[21]I. Joseph, R. A. Moyer, T. E. Evans, M. J. Schaffer, A. M. Runov, R. Schneider, S. V. Kasilov, M. Groth, and M. E. Fenstermacher, J. Nucl. Mater. **363–365**, 591 (2007).
[22]T. E. Evans, C. J. Lasnier, D. N. Hill, A. W. Leonard, M. E. Fenstermacher, T. W. Petrie, and M. J. Schaffer, J. Nucl. Mater. **220–222**, 235 (1995).
[23]T. Eich, A. Herrmann, J. Neuhauser, and ASDEX Upgrade Team, Phys. Rev. Lett. **91**, 195003 (2003).
[24]T. Eich, A. Herrmann, J. Neuhauser, R. Dux, J. C. Fuchs, S. Günter, L. D. Horton, A. Kallenbach, P. T. Lang, C. F. Maggi, M. Maraschek, V. Rohde, W. Schneider, and ASDEX Upgrade Team, Plasma Phys. Controlled Fusion **47**, 815 (2005).
[25]T. E. Evans, J. H. Yu, M. W. Jakubowski, O. Schmitz, J. G. Watkins, and R. A. Moyer, J. Nucl. Mater. **390–391**, 789 (2009).
[26]V. A. Izzo, I. Joseph, R. A. Moyer, T. E. Evans, M. E. Fenstermacher, T. H. Osborne, L. L. Lao, and P. B. Snyder, IAEA Fusion Energy Conference, Geneva Switzerland, 2008, Paper No. TH/P4-19, http://www.fec2008.ch.
[27]H. R. Strauss, L. Sugiyama, G. Y. Park, C. S. Chang, S. Ku, and I. Joseph, Nucl. Fusion **49**, 055025 (2009).
[28]S. Ku, H. Baek, and C. S. Chang, Phys. Plasmas **11**, 5626 (2004).
[29]L. E. Sugiyama, W. Park, H. R. Strauss, S. R. Hudson, D. Stutman, and X.-Z. Tang, Nucl. Fusion **41**, 739 (2001).
[30]L. Sugiyama and M3D Team, J. Phys.: Conf. Ser. **180**, 012060 (2009).
[31]I. B. Bernstein, E. A. Frieman, M. D. Kruskal, and R. M. Kulsrud, Proc. R. Soc. London, Ser. A **244**, 17 (1958).
[32]R. L. Dewar and A. H. Glasser, Phys. Fluids **26**, 3038 (1983).
[33]J. W. Connor, R. J. Hastie, H. R. Wilson, and R. L. Miller, Phys. Plasmas **5**, 2687 (1998).
[34]S. Yu. Medvedev, A. Degeling, Y. Martin, O. Sauter, and L. Villard, Europhys. Conf. Abstr. **27A**, 3.129 (2003); S. Yu. Medvedev, A. A. Ivanov, A. A. Martynov, Yu. Yu. Poshekhonov, A. W. Degaling, J. B. Lister, Y. R. Martin, O. Sauter, and L. Villard, Europhys. Conf. Abstr. **28G**, 2.147 (2004).
[35]H. R. Wilson, P. B. Snyder, G. T. A. Huysmans, and R. L. Miller, Phys. Plasmas **9**, 1277 (2002).
[36]P. B. Snyder, H. R. Wilson, J. R. Ferron, L. L. Lao, A. W. Leonard, T. H. Osborne, A. D. Turnbull, D. Mossessian, M. Murakami, and X. Q. Xu, Phys. Plasmas **9**, 2037 (2002).
[37]G. T. A. Huysmans, S. E. Shaparov, A. B. Mikhailovskii, and W. Kerner, Phys. Plasmas **8**, 4292 (2001).
[38]P. B. Snyder, H. R. Wilson, and X. Q. Xu, Phys. Plasmas **12**, 056115 (2005).
[39]H. R. Strauss, L. Sugiyama, C. S. Chang, G. Park, S. Ku, W. Park, J. Breslau, and S. Jardin, Proceedings of the IAEA FEC, 2006, Paper No. TH/P8-6.
[40]NIMROD ELM results for the DOE Milestone in 2005, FY05 Milestone Reports, 4th Quarter, 2005, http://w3.pppl.gov/cemm/milestones.html.
[41]G. T. A. Huysmans and O. Czarny, Nucl. Fusion **47**, 659 (2007).
[42]N. Mizuguchi, R. Khan, T. Hayashi, and N. Nakajima, Nucl. Fusion **47**, 579 (2007).
[43]W. Park, E. V. Belova, G. Y. Fu, X. Z. Tang, H. R. Strauss, and L. E. Sugiyama, Phys. Plasmas **6**, 1796 (1999).
[44]L. E. Sugiyama and W. Park, Phys. Plasmas **7**, 4644 (2000).
[45]L. L. Lao, H. E. St. John, Q. Peng, J. R. Ferron, E. J. Strait, T. S. Taylor, W. H. Meyer, C. Zhang, and K. I. You, Fusion Sci. Technol. **48**, 968 (2005).
[46]D. M. Thomas, A. W. Leonard, R. J. Groebner, T. H. Osborne, T. A. Casper, P. B. Snyder, and L. L. Lao, Phys. Plasmas **12**, 056123 (2005).
[47]T. E. Evans, R. A. Moyer, J. G. Watkins, T. H. Osborne, P. R. Thomas, M. Becoulet, J. A. Boedo, E. J. Doyle, M. E. Fenstermacher, K. H. Finken, R. J. Groebner, M. Groth, J. H. Harris, G. L. Jackson, R. J. La Haye, C. J. Lasnier, S. Masuzaki, N. Ohyabu, D. G. Pretty, H. Reimerdes, T. L. Rhodes, D. L. Rudakov, M. J. Schaffer, M. R. Wade, G. Wang, W. P. West, and L. Zeng, Nucl. Fusion **45**, 595 (2005).
[48]T. E. Evans, M. E. Fenstermacher, R. A. Moyer, T. H. Osborne, J. G. Watkins, P. Gohil, I. Joseph, M. J. Schaffer, L. R. Baylor, M. Bécoulet, J. A. Boedo, K. H. Burrell, J. S. deGrassie, K. H. Finken, T. Jernigan, M. W. Jakubowski, C. J. Lasnier, M. Lehnen, A. W. Leonard, J. Lonnroth, E. Nardon, V. Parail, O. Schmitz, B. Unterberg, and W. P. West, Nucl. Fusion **48**, 024002 (2008).
[49]A. Jameson, Int. J. Comput. Fluid Dyn. **4**, 171 (1995).
[50]H. Takahashi, E. D. Fredrickson, and M. J. Schaffer, Phys. Rev. Lett. **100**, 205001 (2008).
[51]J. A. Boedo, D. L. Rudakov, E. Hollmann, D. S. Gray, K. H. Burrell, R. A. Moyer, G. R. McKee, R. Fonck, P. C. Stangeby, T. E. Evans, P. B. Snyder, A. W. Leonard, M. A. Mahdavi, M. J. Schaffer, W. P. West, M. E.

Fenstermacher, M. Groth, S. L. Allen, C. Lasnier, G. D. Porter, N. S. Wolf, R. J. Colchin, L. Zeng, G. Wang, J. G. Watkins, T. Takahashi, and DIII-D Team, Phys. Plasmas **12** 072516 (2005).
[52]J. L. Terry, S. J. Zweben, M. V. Umansky, I. Cziegler, O. Grulke, B. LaBombard, and D. P. Stotler, J. Nucl. Mater. **390–391**, 339 (2009).
[53]S. J. Zweben, R. A. Maqueda, J. L. Terry, B. Bai, C. J. Boswell, C. E. Bush, D. DIppolito, E. D. Fredrickson, M. Greenwald, K. Hallatschek, S. Kaye, B. LaBombard, R. Maingi, J. Myra, W. M. Nevins, B. N. Rogers, D. P. Stotler, J. Wilgen, and X. Q. Xu, Europhys. Conf. Abstr. **26B**, 3.220 (2002).
[54]H. R. Wilson and S. C. Cowley, Phys. Rev. Lett. **92**, 175006 (2004).
[55]R. Maingi, M. G. Bell, E. D. Fredrickson, K. C. Lee, R. J. Maqueda, P. Snyder, K. Tritz, S. J. Zweben, R. E. Bell, T. M. Biewer, C. E. Bush, J. Boedo, N. H. Brooks, L. Delgado-Aparicio, C. W. Domier, D. A. Gates, D. W. Johnson, R. Kaita, S. M. Kaye, H. W. Kugel, B. P. LeBlanc, N. C. Luhmann, Jr., J. E. Menard, D. Mueller, H. Park, R. Raman, A. L. Roquemore, S. A. Sabbagh, V. A. Soukhanovskii, T. Stevenson, and D. Stutman, Phys. Plasmas **13**, 092510 (2006).
[56]H. R. Strauss, Phys. Plasmas **2**, 1229 (1995).
[57]A. B. Hassam, T. M. Antonsen, J. F. Drake, and C. S. Liu, Phys. Rev. Lett. **66**, 309 (1991).
[58]E. J. Strait, T. A. Casper, M. S. Chu, J. R. Ferron, A. Garofalo, C. M. Greenfield, R. J. La Haye, L. L. Lao, E. A. Lazarus, R. L. Miller, G. A. Navratil, C. Ren, B. W. Rice, I. Semenov, A. C. C. Sips, F. X. Soldner, B. W. Stallard, T. S. Taylor, A. D. Turnbull, and DIII-D Team, Phys. Plasmas **4**, 1783 (1997).
[59]M. E. Fenstermacher, T. H. Osborne, A. W. Leonard, P. B. Snyder, D. M. Thomas, J. A. Boedo, T. A. Casper, R. J. Groebner, M. Groth, M. A. H. Kempenaars, A. Loarte, G. R. McKee, W. M. Meyer, G. Saibene, M. A. VanZeeland, X. Q. Xu, L. Zeng, and DIII-D Team, Nucl. Fusion **45**, 1493 (2005).
[60]J. H. Yu, J. A. Boedo, E. M. Hollmann, R. A. Moyer, D. L. Rudakov, and P. B. Snyder, Phys. Plasmas **15**, 032504 (2008).
[61]A. Kirk, H. R. Wilson, G. F. Counsell, R. Akers, E. Arends, S. C. Cowley, J. Dowling, B. Lloyd, M. Price, M. Walsh, and MAST Team, Phys. Rev. Lett. **92**, 245002 (2004).
[62]B. Koch, A. Herrmann, A. Kirk, H. Meyer, J. Dowling, J. Harhausen, J. Neuhauser, H. W. Müller, W. Bohmeyer, G. Fussmann, AUG Team, and MAST Team, J. Nucl. Mater. **363–365**, 1056 (2007).
[63]M. W. Jakubowski, W. Fundamenski, G. Arnoux, Th. Eich, R. A. Pitts, D. Reiter, R. C. Wolf, and JET-EFDA Contributors, J. Nucl. Mater. **390–391**, 781 (2009).
[64]R. J. Maqueda, R. Maingi, and NSTX Team, Phys. Plasmas **16** 056117 (2009).
[65]R. J. Maqueda, R. Maingi, J.-W. Ahn, and NSTX Team, J. Nucl. Mater. **390–391**, 843 (2009).
[66]T. E. Evans, R. K. W. Roeder, J. A. Carter, and B. I. Rapoport, Contrib. Plasma Phys. **44**, 235 (2004).
[67]P. M. Oppeneer, Phys. Lett. **104A**, 207 (1984), and references therein.
[68]V. A. Vladimirov and H. K. Moffatt, J. Fluid Mech. **283**, 125 (1995); V. A. Vladimirov, H. K. Moffatt, and K. I. Ilin, *ibid.* **329**, 187 (1996).
[69]A. B. Rechester and M. N. Rosenbluth, Phys. Rev. Lett. **40**, 38 (1978).
[70]H. R. Strauss, Phys. Fluids **24**, 2004 (1981).
[71]J. S. deGrassie, R. J. Groebner, K. H. Burrell, and W. M. Solomon, Nucl. Fusion **49**, 085020 (2009).
[72]J. Rapp, W. Fundamenski, L. C. Ingesson, S. Jachmich, A. Huber, G. F. Matthews, P. Morgan, M. F. Stamp, and JET-EFDA Contributors, Plasma Phys. Controlled Fusion **50** 095015 (2008).